Author for correspondence:
S. R. Stock
e-mail: s-stock@northwestern.edu

THE ROYAL SOCIETY
PUBLISHING

Bioapatite in shark centra studied by wide-angle and by small-angle X-ray scattering

J. S. Park[1], J. D. Almer[1], K. C. James[2], L. J. Natanson[3] and S. R. Stock[4]

[1]The Advanced Photon Source, Argonne National Laboratory, Lemont, IL 60439, USA
[2]Southwest Fisheries Science Center, National Marine Fisheries Service, NOAA, La Jolla, CA, USA
[3](retired) Northeast Fisheries Science Center, National Marine Fisheries Service, NOAA, Narragansett, RI, USA
[4]Department of Cell and Developmental Biology, Feinberg School of Medicine, and Simpson Querrey Institute, Northwestern University, Chicago, IL, USA

SRS, 0000-0002-8886-4035

Members of subclass Elasmobranchii possess cartilage skeletons; the centra of many species are mineralized with a bioapatite, but virtually nothing is known about the mineral's organization. This study employed high-energy, small-angle X-ray scattering (SAXS) and wide-angle X-ray scattering (WAXS, i.e. X-ray diffraction) to investigate the bioapatite crystallography within blocks cut from centra of four species (two carcharhiniform families, one lamniform family and 1-ID of the Advanced Photon Source). All species' crystallographic quantities closely matched and indicated a bioapatite closely related to that in bone. The centra's lattice parameters a and c were somewhat smaller and somewhat larger, respectively, than in bone. Nano-crystallite sizes (WAXS peak widths) in shark centra were larger than typical of bone, and little microstrain was observed. Compared with bone, shark centra exhibited SAXS D-period peaks with larger D magnitudes, and D-period arcs with narrower azimuthal widths. The shark mineral phase, therefore, is closely related to that in bone but does possess real differences which probably affect mechanical property and which are worth further study.

1. Introduction

Elasmobranchii include the sharks, skates and rays, and the vertebrae and their main load-bearing components, the centra and other skeletal components consist of cartilage (types I and II collagen, proteoglycans [1,2]). All sharks known to the authors from orders Carcharhiniformes and Lamniformes contain centra whose cartilage is reinforced with biomineral, albeit a few species are only partially mineralized. These vertebrae experience tens of millions of cycles of swimming-related loading [3], this loading alternates compression of the left side of the centra with compression of the right side (figure 1*a*) and strain magnitudes can reach 3–8% [5], an enormous level for mineralized tissue[1], especially considering that the centra do not appear to have a remodelling mechanism like that in bone for removing accumulated microdamage.

Each centrum contains an hourglass-shaped structure (the corporus calcerea, in geometrical terms, a double napped right cone) whose axis is parallel to the axis of the vertebral column. The cranial and caudal cone walls are supported by the intermedialia. Intermedialia structure differs between lamniforms and carcharhiniforms: the former possesses two dozen or more, relatively thin plates (lamellae, figure 1*b*) and the latter four much thicker wedges (figure 1*c*). Loading is along vertebral column axis ('vca' in figure 1, i.e. the centrum's axis) and consists of asymmetric compression (figure 1*a*). Simple compression stress–strain curves have been measured from intact centra from lamniforms and from carcharhiniforms [7], and, to the present authors, the data look more like that of an elastomer than a mineralized tissue like bone.
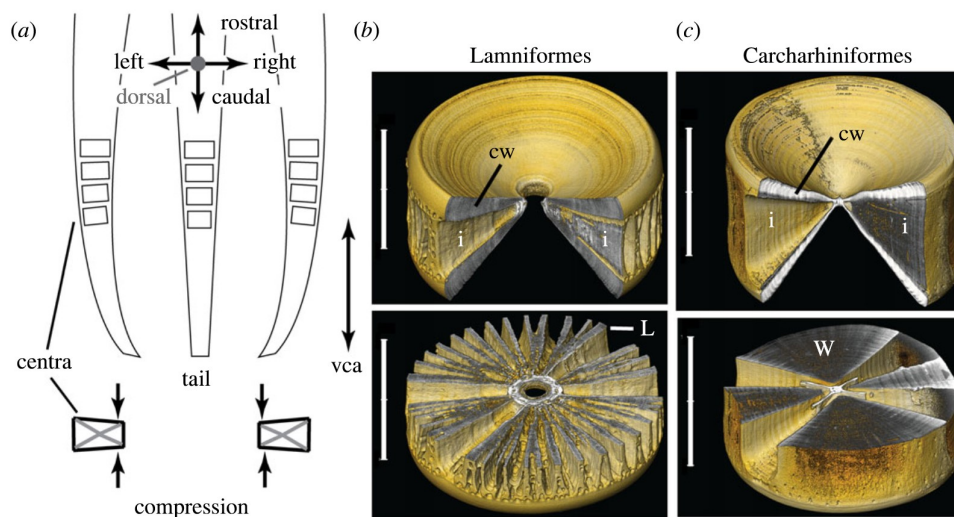
Figure 1. (*a*) Schematic of the swimming motion of a shark showing the caudal portion of the animal and centra within. The anatomical directions are indicated at the top of the panel. In the top portion of the panel and from left to right, the tail is shown swept to the left, at a neutral orientation and swept to the right. The bottom panel shows the resulting compression of a centrum; the grey 'x' within each of these centra represents the projection of the double cone (corpus calcera). The vertebral column axis 'vca' is labelled. (*b,c*) Laboratory microCT-derived three-dimensional rendering of lamniform and of carcharhiniform shark vertebral centra, respectively, derived from data in Morse *et al*. [4]. These are from a shortfin mako and a sandbar shark, respectively, and the internal structures are similar to but not identical to those in the blocks examined in the present study. The top row shows a view from above of each centra; a sector facing the viewer is rendered transparent so that the cone wall cross-section can be seen. The bottom row shows the same volume but with the clipping plane through the midplane of each centra; this allows the intermedialia structure to be appreciated. The scale bars at the left of each image are 10 mm. L—lamella, W—wedge, cw—cone wall, i—intermedialia.

The two major types of mineralized cartilage in sharks, vertebral centra and tesserae (e.g. in the jaws), form via different mineralization processes [8], and Urist [9] and Dean *et al*. [10] found that the mineral in both tissues is a form of hydroxyapatite (hAp) similar to the bioapatite reinforcing bone, a biocomposite with a different matrix, type I collagen. Since the data of this paper were collected, energy-dispersive (X-ray) diffraction (EDD) of intact shark centra confirmed recently that bioapatite was the mineral phase present and revealed interesting crystallographic texture [11,12]. These studies did not report lattice parameters, and it is unclear whether the mineral is hAp (a relatively pure phase containing low levels of impurities) or carbonated apatite like that found in bone and tooth. For this reason, the mineral phase in shark centra is designated 'bioapatite' to avoid implying a certain composition range. One goal of the present study is to measure accurate lattice parameters for several sharks from Carcharhiniformes and Lamniformes. Because tesserae [13] and bone, another collagen-based mineralized tissue, both are hierarchically structured, it is reasonable to hypothesize that similar ranges of structure make up the tissue of shark centra, and describing mineral phase nano-organization is the second goal of the present study.

Wide-angle X-ray scattering (WAXS, i.e. X-ray diffraction) and small-angle X-ray scattering (SAXS) are used here to quantify bioapatite lattice parameters and other nanostructural characteristics for several shark centra. X-rays scatter from the atoms within a specimen, and this scattering reinforces along certain directions depending on the X-ray wavelength and on the periodicities within and orientation of the scatterers. The reinforced scattering produces peaks in intensity described by Bragg's law (see equations (2.1) and (2.2) in Materials and methods). In WAXS, the periodicities are those of the atoms within the unit cells of any

crystalline phase present, and the directionality and relative intensity of different diffraction peaks provide a 'fingerprint' of the material; see [14] for example. Typically, periodicities investigated with WAXS range from 0.5 to 10 Å. In SAXS, the scattering is from an array of objects like nanoparticles (or macromolecules) with spacings approximately 5–100 nm, and directionality of scattered intensity indicates concentration of scatterer orientations. The terms 'wide angle' and 'small angle' are relative terms because the magnitude of the angles depends on the X-ray wavelength (Bragg's law, equations (2.1) and (2.2) below).

Many mineralized tissues have been studied with WAXS and/or SAXS including mammalian bone, e.g. [15], and fish bone, e.g. [16,17]). Because the present WAXS/SAXS study is the first on shark centra bioapatite, and shark tesserae diffraction studies [10,18] provide limited information, we use bone and its well-known structural hierarchies [19] as a template against which to compare the shark data. The bioapatite crystal system is hexagonal with lattice parameters a and c, and bone's bioapatite contains significant carbonate which affects the values of a and c; see [20]. Bone's type I collagen matrix is reinforced by an array of bioapatite nanoparticles (crystallites), and WAXS peak width analysis provides a robust measure of these crystallites' sizes [15] and of microstrain (gradients in lattice parameters within the irradiated volume), if present. Microstrain is typically significant in bone and, if ignored, leads to erroneous values of crystallite size [14]. Peak positions in WAXS patterns allow precise measurement of lattice parameters and inference of compositional variation, e.g. [20], something which may relate to physiology of bioapatite production.

In long bones, collagen fibrils align along the bones' axes, the direction of principal stress, and the bioapatite c-axes tend to be parallel to the collagen fibril axes in bone. The tendency

Table 1. List of species from which vertebral tissue was studied. Abbreviations used for the orders (families) are Carcharhiniformes = C (Carcharhinidae = Ca, Sphyrnidae = Sph); Lamniformes = L (Lamniidae = La).

shark	order / family	sample id	orient	block i.d.
Galeocerdo cuvier	C / Ca	T355	axial	Tg2c
tiger shark			axial	Tg2d
Sphyrna mokarran	C / Sph	GHH29	axial	f
great hammerhead			nappe	m
Sphyrna lewini	C / Sph	SCH322	axial	9
scalloped hammerhead			vertex	4
Lamna nasus	L / La	LN670	axial	L2c
porbeagle			axial	L2d

of a certain crystallographic axis to lie along a specific direction in a specimen is termed crystallographic texture, and texture in long bones' cortices results in elastic moduli along the longitudinal anatomical direction being 1.8 times greater than that for the transverse direction [21]. As described below, such crystallographic texture is readily quantified in both WAXS and SAXS patterns. For WAXS of bone, texture is most evident in azimuthal intensity variation along 00.2 and 00.4 diffraction rings.[2] In SAXS, well-defined peaks are present: these peaks' periodicity relates to the mean bioapatite particle spacing along the collagen fibre axis, the *D*-period, e.g. [15], and directionality of the scattered intensity, like in WAXS, also reveals texture of the mineral phase.

The present study reports results of WAXS and SAXS on blocks cut from centra of four different species (two families of Carcharhiniformes and one family of Lamniformes). These results are the first on multiple levels of nanostructure of the subclass Elasmobranchii and fill, therefore, a very important gap in our knowledge of biomineralization. The WAXS results (and their importance) include

1) determination of bioapatite lattice parameters (lattice parameters different from those of bioapatites of mammals indicate different composition and different physiological processes during biomineralization),
2) presence and type of bioapatite crystallographic texture (presence/absence of texture and its strength can indicate evolution and/or development in response to *in vivo* loading),
3) bioapatite crystallite size and microstrain (the size of reinforcing particles affects the strength and fracture resistance of composite materials including those from nature).

The SAXS results include

4) values of *D*-period which is the mean spacing of the bioapatite nanoparticles (the spacing and arrangement of reinforcing particles affects composite mechanical properties), and
5) the extent of preferred orientation of bioapatite nanoparticles and its direction relative to the vertebrae's anatomical axes (see item 2 above).

The two goals of this exploratory study are to uncover commonalities/differences between the shark species and to investigate the extent to which the shark mineral phase and mineral particle arrangement are similar to the bioapatite and its nanoparticles' arrangement in bone, the most extensively studied collagen-based bioapatite composite.

2. Materials and methods

Vertebral mineralized tissue from one adult each of four species was studied: *Galeocerdo cuvier* (tiger shark), *Sphyrna mokarran* (great hammerhead), *S. lewini* (scalloped hammerhead), and *Lamna nasus* (porbeagle). The first three are carcharhiniforms (two families and three species), and last is a lamniform shark (table 1, two blocks from each species). Each frozen abdominal centrum (one per species) was clamped in the sample holder of an Isomet 1000 slow speed saw (Buehler, Lake Bluff, IL, USA), and a diamond wafering blade and water irrigation were used to cut a series of approximately 2.6 mm thick slabs from each centrum (orientations indicated in figure 2*a*). These slabs were placed briefly in water until the slab could be cut into bars. Some bars were cut with the wafering saw and some with a razor blade tapped with a hammer; synchrotron microcomputed tomography (microCT), data not shown, revealed cutting damage extended no farther than a few tens of micrometres into each block. The spacing and orientation of these cuts varied from specimen to specimen (figure 2*b*; see electronic supplementary material, figure S1 for more detailed information). Six of the blocks were 'axial', i.e. with their longest axis parallel to the vertebral column axis (table 1). Another block was cut in the 'nappe' orientation, long direction along the cone's nappe and contained cone wall tissue: contrast in sections used for age determination differs between cone and intermedialia tissue [22], and scans of the axial blocks were expected to sample intermedialia tissue. One block was cut with a transverse axis and contained the cones' vertices, the earliest portion of the centrum to form; examining this answer whether the bioapatite differed from later formed material. The bars were kept wet and placed into small plastic tubes filled with 50% ethanol and wedged into place with polymer foam.

The blocks were studied at beamline 1-ID, the Advanced Photon Source (APS) with 71.676 keV photons and with a 0.120×0.120 mm beam (figure 2*c*); there is an aperture within the WAXS detector array which allows WAXS and SAXS patterns to be collected simultaneously. The distance of the specimen to the WAXS detector 2 (a GE-41RT detector, with 0.200 mm isotropic pixels, oriented to capture a mostly horizontal portion of the Debye cone) was nominally 1.650 m; the sample–SAXS detector (Pixirad2, with 0.056 mm isotropic pixel dimensions) separation was nominally 6.000 m. For WAXS, detector panel 2 collected diffracted intensity from a range of bioapatite crystals spanning the
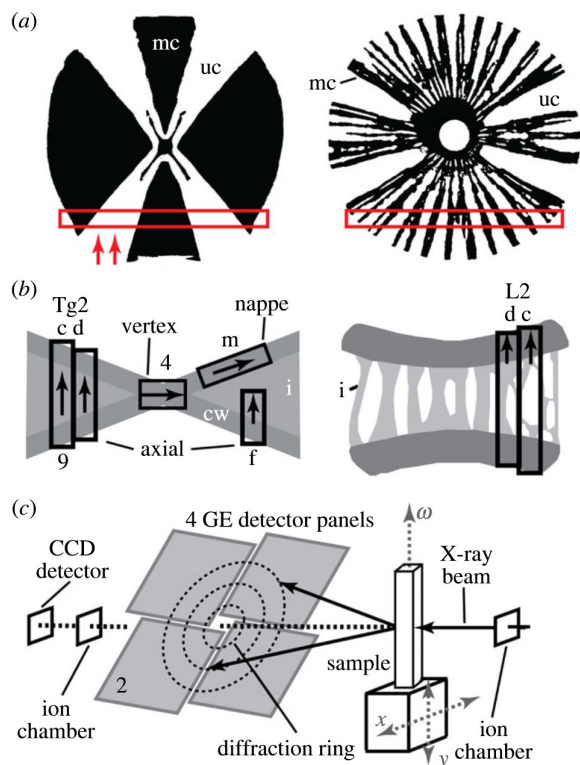
Figure 2. (*a*) Transverse cross-sections near the centre of a carcharhiniform centrum (left, blue shark) and of a lamniform centrum (right, shortfin mako). Mineralized cartilage 'mc' and unmineralized cartilage 'uc' are indicated. The red boxes indicate the position of the sections from which the blocks in this study were cut, and the red arrows in the carcharhiniform cross-section point to the position of blocks Tg2c and Tg2d from the tiger shark. (*b*) Schematics of a longitudinal section of a carcharhiniform centrum (left) and a lamniform centrum (right) labelled with the positions of blocks cut from the section; the direction of the arrow indicates the vertical orientation of the block during WAXS/SAXS scanning. The axially oriented blocks were Tg2c, Tg2d, L2c, L2d, 9 and f. The vertex block and nappe blocks were 4 and m, respectively. Note that the lamniform section is derived from microCT data from a shortfin mako with the smaller diameter porosity not shown; the amount of void space in the intermedialia varies considerably across the section (bar L2c contains considerable interlamellar space whereas L2d contains more solid). (*c*) Schematic of the data collection at beamline 1-ID, APS, with the following indicated: positioning axes *x* and *y*, specimen rotation axis ω, WAXS detector (GE panel 2) and SAXS detector (CCD detector).

horizontal direction. For SAXS, the incident beam was positioned near one corner of the detector; scattering over a full 360° azimuthal range could be collected out to the second-order *D*-period peak and the azimuthal angular range decreased at higher angles.

The data were collected under a mail-in mechanism: APS SARS-CoV-2 site access restrictions prevented the corresponding author (S.R.S.) from being present. The consequence was that the area scanned in each specimen could not be adjusted by the experimenter (S.R.S.) familiar with the specimen's anatomical position of origin. Each block inside its tube and surrounded by ethanol was placed on the sample positioner with the block's long axis vertical (arrow in figure 2*b*), parallel with the instrument's ω- rotation axis (figure 2*c*). The block was positioned with the beam near the centre of the specimen's long axis. The goal was to sample the intermedialia of each block except for nappe-oriented block (m) which consisted of cone tissue and for the cone vertex block (4) which was the complex structure where the cones come together and contained the

earliest formed mineral; as discussed below cone wall material was sampled in blocks other than m.

At ω = 0° (vertical axis position, figure 2*c*), each specimen was translated across the beam with SAXS patterns recorded (3 s exposure) every 59–63 μm, depending on the scan, and with the WAXS pattern recorded as an average for the entire scan. The goal was not to map positional differences but to ensure collection of patterns representative of each block. Note that the WAXS and SAXS measurements averaged structure within the approximately 3 mm sample thickness. After data were collected for each block with ω = 0°, the specimen was rotated to ω = 180°, and the translation series recorded for a second time. For each position, comparison of diffraction patterns (WAXS) recorded at these two angles allows very precise correction for displacements of the centre of mass from the nominal sample position [23].

Slight detector tilts were corrected, and the precise distance from the specimen rotation axis to each detector were determined by collecting patterns from two standards at ω = 0° and at ω = 180°. A ceria standard (NIST SRM 674a) and an Au-coated Si grating were employed for WAXS and SAXS, respectively. After tilt correction, the WAXS and SAXS patterns (concentric rings in the radial coordinate system, azimuth η versus radius from the incident beam position) were converted a Cartesian coordinate system (η along the *y*-axis and ring radius along the *x*-axis, converting the rings into straight lines) and then to azimuth versus *d*-spacing (WAXS) or versus *D*-period (SAXS) using Bragg's law,

$$\lambda = 2d_{hkl} \sin \theta \quad \text{or} \quad (2.1)$$

$$n\lambda = 2D \sin \theta, \quad (2.2)$$

respectively, where λ is the X-ray wavelength, hkl are the indices of the different periodicities within the crystal lattice, *n* is the order of scattering peak (periodicities of *D*, *D*/2, *D*/3, ... often produce measurable intensities) and θ is the Bragg angle, e.g. [14]. Azimuth η = 180° is horizontal and η = 90° is vertical and parallel to the ω rotation axis. After azimuthal integration, the discrete bioapatite WAXS peaks 00.2, 22.2, 00.4 and 21.3 were fit with a pseudoVoigt function with a mixture of 50% Lorentzian–50% Gaussian character, and $d_{20.1}$, $d_{00.2}$, $d_{22.2}$, $d_{00.4}$ and $d_{21.3}$ were calculated from the peak positions for both ω = 0° and ω = 180°.[3] The average of *d*(ω = 0°) and *d*(ω = 180°) was computed in order to eliminate any effect of slight variation between each sample's centre of mass and the rotation centre [23]. After these data were tabulated, an unusually large variation in $d_{00.2}$ was noted, and fitting was repeated including the nearby 20.1 peak. Because peak position accuracy generally increases at larger angles/radii from the detector centre, lattice parameter *c* was calculated from $d_{00.4}$ and lattice parameter *a* from the value of *c* and the values of $d_{22.2}$ and $d_{21.3}$ using the normal formulae [14].

The full-width at half-maximum intensity (FWHM) were determined from the fit of the 20.1, 00.2, 22.2, 21.3 and 00.4 peaks. The coherently scattering domain size (crystallite size $L_{hk.l}$) was calculated from the Scherrer equation,

$$B_{hk.l} = \frac{(K \lambda)}{(L_{hk.l} \cos \theta)}, \quad (2.3)$$

where $B_{hk.l}$ is the experimentally measured peak FWHM (rad 2θ) corrected for instrumental broadening and *K* = 0.9 [14]. Note that common domain shapes have 0.85 < *K* less than 0.95; the use of 0.9 introduces an error no greater than 10%. Instrumental broadening was measured with a LaB₆ reference specimen (NIST SRM 660a) and was constant at about 2.5 detector pixels over the 2θ range studied. Note that if *B* * cos θ varies significantly with sin θ, then microstrain (gradients or ranges of *d*-spacing within the volume sampled by the X-ray beam) is present and broadens the diffraction peaks [14], and equation (2.3) is accurate for crystallite sizes only when one accounts for microstrain. Unlike in bone specimens, the shark specimens showed negligible microstrain.
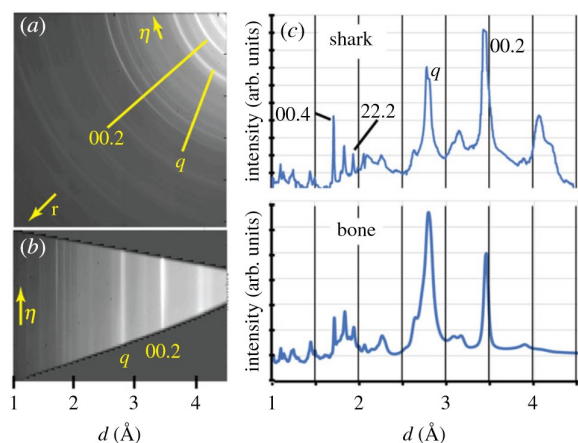
Figure 3. (a) WAXS pattern of block Tg2d showing the two-dimensional distribution of intensities intercepted by GE detector 2. The 00.2 and quadruplet (q, unresolved 21.1, 11.2, 30.0 and 20.2) reflections are labelled, as are the radial r and azimuthal η directions. In (a,b), the lighter the pixel, the greater the intensity. (b) Cartesian transformed pattern from (a) showing azimuth vertically and d horizontally. (c) Azimuthally averaged plots of intensity (in arbitrary units) as a function of d for shark mineralized tissue (top) and for canine bone (bottom). The 22.2 and 00.4 reflections are also labelled.

For the SAXS patterns, values of D at $\omega = 0°$ and $\omega = 180°$ were averaged to determine each block's value. In a representative block (Tg2c, tiger shark and axial orientation), SAXS patterns from 30 positions were averaged to allow the higher order D-period peaks to be characterized. The D-period peaks from the shark centrum blocks were arcs, and the azimuthal FWHM of the D-period arcs ($\Delta\eta_D$) were quantified. Although the goal of these experiments was not to determine positional variations within the centra, this variation affected interpretation of the results, and videos were made of the series of SAXS patterns (each frame was a successive position) for each block.

3. Results

A typical WAXS pattern appears in figure 3a in the as-collected, polar coordinate system (radius r versus azimuthal angle η) and in figure 3b after transformation to Cartesian coordinates (azimuth η versus d-spacing). The diffraction rings are continuous, and, except for the 00.2 and 00.4 rings, there is little azimuthal variation of intensity visible in the angular range sampled by the detector. The one-dimensional WAXS pattern extracted from figure 3b by azimuthal averaging is presented in figure 3c and is very similar to the pattern for canine bone shown for comparison. Like the two-dimensional pattern (figure 3a), the one-dimensional WAXS pattern is typical of the other blocks of shark centra. The 00.2 and quadruplet 'q' of closely spaced 21.1, 11.2, 30.0 and 20.2 reflections are indicated; the quadruplet peaks, nominally $d = 2.816, 2.776, 2.734$ and 2.628 Å, respectively, from powder diffraction file entry 86–1201, are characteristic of a hexagonal crystal system. The quadruplet peaks in the pattern from shark mineralized cartilage and that from bone (figure 3c) cannot be resolved, a common observation for mineralized, bioapatite-containing tissue except tooth enamel, e.g. [15,24]. Note that instrumental broadening differed between the patterns of figure 3c and the 00.2 peak widths cannot be compared by inspection.

Table 2 shows that all four shark species (and all eight blocks) had virtually identical d-spacings for five peaks that had appreciable intensity and which did not suffer serious overlaps with other strong peaks. These were the 20.1, 00.2, 22.2, 21.3 and 00.4 reflections. Lattice parameters a and c for all eight samples also differed very little (table 3), and the mean lattice parameters were $c = 6.894 \pm 0.002$ Å and $a = 9.420 \pm 0.009$ Å for all eight specimens.[4] Expressed another way, the standard deviation of c was about 0.03% of the mean and of a was about 0.1% of the mean.

Table 2 also gives peak widths for 20.1, 00.2, 22.2, 21.3 and 00.4. As shown in table 3, the bioapatite crystallite size L_c along the c-axis direction is similar for seven of the eight samples (range $53 \leq L_c$ (nm) ≤ 65 with a mean of 60 ± 7 nm and one outlier of 73 nm for Tg2c, tiger shark, axially oriented block). Crystallite sizes for one mixed $hk.l$ index peak, 22.2, are also tabulated in table 3 and were similar for all blocks except one of the tiger shark blocks (range $25 \leq L_{22.2}$ (nm) ≤ 38 with mean 33 ± 11 nm and one outlier of 56 nm for Tg2c, tiger shark, axially oriented block).

Crystallographic texture in mineralized tissues typically manifests in azimuthal intensity variation in 00.l diffraction rings. With only detector panel 2 recorded, the azimuthal range of the 00.2 reflection is too small to reveal texture, but the 00.4 reflection has a range $\Delta\eta \sim 65°$ (figure 3b), and this suffices to reveal the presence and absence of texture. In figure 3b (Tg2d, tiger shark intermedialia, axially oriented block), the 00.4 ring is visibly more intense at $\eta = 130°$ than at $\eta = 180°$. Quantitatively, $I_{00.4} \sim 130$ arb. units with a background intensity of approximately 90 arb. units at $\eta = 130°$ whereas $I_{00.4} \sim 110$ arb. units with background intensity of approximately 100 arb. units at $\eta = 180°$.

Figure 4 shows a typical SAXS pattern from a centrum block. The two-dimensional pattern of figure 4a shows two strong D-period peaks (vertical white arrows) and additional, higher order peaks at the edge of visibility. At azimuths normal to those of the D-period peaks, a halo of strong scattering extends well beyond the two D-period peaks (figure 4a); this halo is quite narrow azimuthally. Figure 4b shows a plot of SAXS intensity versus q, the magnitude of the scattering vector, for sample Tg2c (tiger shark, axial block); this plot sums 30 patterns across the specimen and is based on intensity integration over azimuths $\pm10°$ from horizontal. Six regularly spaced D-period peaks are clearly visible in figure 4b; the spacing between peaks is nearly identical and corresponds to an average $D = 66.8$ nm.

Figure 5 shows a representative SAXS pattern for each of the blocks; the patterns recorded during translation appear in the electronic supplementary material, videos. In each pattern, the orientation of the vertebral column axis is indicated by the green arrow in the upper left corner, and the number in the lower right corner gives the maximum intensity for that panel. Blocks from all four species produce D-period arcs; the axis of symmetry of one pair of arcs is indicated by the yellow arrow in panel Tg2d. A single pair of arcs (on either side of the incident beam) appears for the tiger shark blocks (Tg2c and Tg2d), for one block of the scalloped hammerhead (9) and for one porbeagle block (L2d). The SAXS patterns of two blocks, f (great hammerhead) and 4 (scalloped hammerhead), show two pairs of D-period arcs; these are labelled '1' and '2' and occur at azimuths about 90° apart. The arcs from great hammerhead block m are too faint to reliably quantify (frame 868 of electronic supplementary material, video S4 shows one

Table 2. Summary of mean d-spacings (Å) for d_1, d_2, d_3, d_4 and d_5 ($hk.l$ 20.1, 00.2, 22.2, 21.3 and 00.4, respectively) for the four species and eight blocks scanned and of peak FWHM in units of detector pixels. The sample column gives the sample designation, and the column 'orient' gives the anatomical orientation of the block. The mean values and their standard deviations (s.d.) over all samples appear at the bottom of the table.

shark	sample	orient	d (Å)					FWHM (pix)				
			20.1	00.2	22.2	21.3	00.4	20.1	00.2	22.2	21.3	00.4
G. cuvier	Tg2c	axial	3.496	3.442	1.945	1.842	1.722	6.8	5.8	7.2	6.8	9.1
	Tg2d	axial	3.494	3.444	1.944	1.842	1.723	8.0	6.3	12.2	6.9	9.5
S. mokarran	f	axial	3.494	3.446	1.943	1.842	1.724	8.2	6.3	11.6	6.8	9.2
	m	nappe	3.495	3.447	1.943	1.842	1.724	7.8	7.0	13.4	7.8	11.5
S. lewini	4	vertex	3.494	3.444	1.946	1.843	1.723	8.0	6.4	12.2	7.4	9.3
	9	axial	3.494	3.444	1.947	1.842	1.724	8.3	7.2	13.4	7.4	10.8
L. nasus	L2c	axial	3.494	3.442	1.943	1.841	1.724	8.0	7.4	13.7	7.9	13.0
	L2d	axial	3.493	3.443	1.943	1.842	1.723	7.8	6.8	11.3	8.6	12.7
		mean	3.494	3.444	1.945	1.842	1.724	7.9	6.7	11.9	7.5	10.7
		s.d.	0.001	0.002	0.002	0.001	0.001	0.5	0.6	2.1	0.6	1.6

Table 3. From WAXS: lattice parameters a and c in Å from 00.4, 22.2 and 21.3 peaks; crystallite size L_c in nm along the hAp c-axis (average of values for 00.2 and 00.4 hAp reflections) and crystallite size $L_{22.2}$ in nm for the hAp 22.2 peak. From SAXS: $\eta_{D\ max}$—azimuthal orientation of the maximum intensity of the D-period peak(s) in degree (°), $\Delta\eta_D$—azimuthal FWHM of the D-period peak(s) in degree (°), N_D—number of D-period peaks quantifiable in a single pattern, D-period values in nm where subscript denotes order of the peak. The superscripts 'a' denote SAXS data where the fit of the D-period peak was poor (sample m); 'b' in the row of mean values indicates means excluding the unreliable SAXS values for sample m. Each block was regarded as an independent sample because we do not assume lattice parameter, crystallite size azimuthal arc widths and invariant within each centrum.

shark	sample	orient	a	c	L_c	$L_{22.2}$	$\eta_{D\ max}$	$\Delta\eta_D$	N_D	D_1	D_3
G. cuvier	Tg2c	axial	9.425	6.890	73	56	176	28	2	67.0	67.0
	Tg2d	axial	9.419	6.894	65	29	156	24	2	67.8	67.0
S. mokarran	f	axial	9.413	6.900	65	29	151	28	2	67.3	67.3
	m	nappe	9.416	6.897	55	25	174[a]	44[a]	1	64.5[a]	–
S. lewini	4	vertex	9.434	6.893	61	29	108	32	2	67.8	67.9
	9	axial	9.431	6.895	56	38	94	30	2	67.8	67.5
L. nasus	L2c	axial	9.410	6.893	53	23	–	–	–	–	–
	L2d	axial	9.414	6.893	53	34	182	29	2	67.2	67.3
		mean	9.420	6.894	60	33		28[b]		67–68[b]	
		s.d.	0.009	0.002	7	11		3			

of the more prominent D-period peaks for this block), and no arcs are visible for porbeagle block L2c.

For most of the blocks, careful examination of the SAXS patterns reveals first- and third-order D-period peaks with intensities high enough to allow quantification of D. Values of D for all of the blocks were between 67 and 68 nm (table 3) except for the block without D-period arcs (L2c) and for block m whose very low-intensity peaks could not be unreliably fit and yielded $D = 64.5$ nm. The azimuthally narrow scattering halo (e.g. the orange arrow in panel Tg2c) contains the highest intensity of each pattern, and the halo appears in the same azimuthal orientation relative to the D-period arcs for all of the samples (about 90° from the centre of the arcs). Although the D-period arcs for some blocks (Tg2c, Tg2d, f, 4 and 9) appear more intense than the others in figure 5, this probably relates to the volume sampled.

Azimuthal FWHM of SAXS D-period peaks is a direct measure of the range of bioapatite nanoparticle (and the underlying cartilage or type I collagen) orientations. If the scatterers are isotropically oriented (i.e. all orientations are equally probable), complete rings result. If certain orientations predominate, this manifests as incomplete rings or arcs of high intensity which indicate the preferred orientations. Therefore, the smaller the value of azimuthal FWHM, the tighter the range of orientations (stronger the crystallographic texture). The array of bioapatite particles in the shark centra have strong preferred orientation: the SAXS D-period peaks for six of the eight blocks (all four species) have narrow azimuthal FWHM with a mean value $\Delta\eta_D = 28 \pm 3°$ (table 3). The low-intensity scattering from the nappe-oriented block of the great hammerhead (m) and axially oriented block of the porbeagle (L2c) prevented measurement of $\Delta\eta_D$. The azimuth
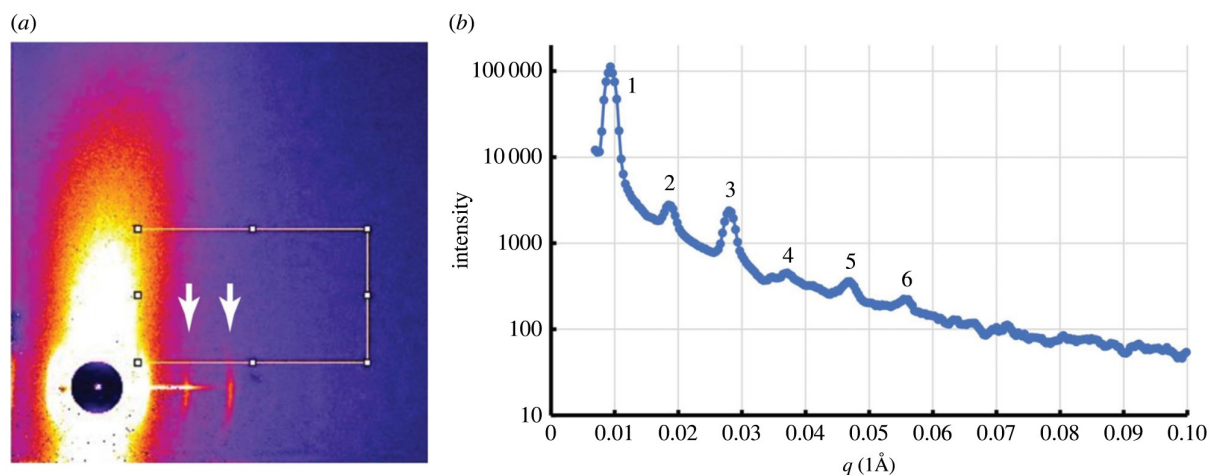
Figure 4. (*a*) Typical two-dimensional SAXS pattern from shark centra block Tg2c with intensity illustrated by colour (in order of decreasing intensity: white, orange, red, purple and indigo). The two vertical white arrows show the strongest *D*-period peaks. (*b*) Plot of intensity as a function of magnitude of the scattering vector *q* using integration over azimuths ± 10° from horizontal; the plot averages 30 patterns collected on sample Tg2c.
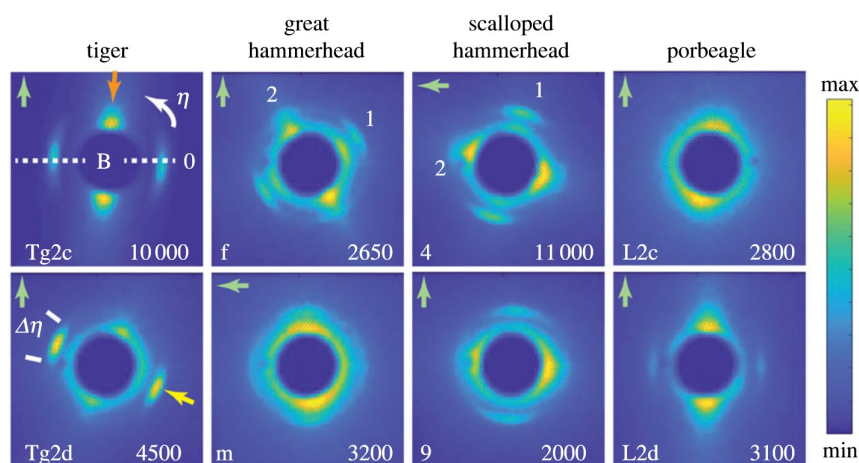
Figure 5. A typical SAXS pattern from each specimen; the area shown is 100 × 100 detector pixels. See also electronic supplementary material, videos S1–S8. Each column consists of patterns from the two blocks of each species' centrum, with the block identified at the lower left of each panel and the maximum intensity (counts) in the pattern at the lower right corner. The green arrow in the upper left corner indicates each block's vertebral column's axis relative to the SAXS detector. The horizontal dashed line labels azimuthal angle $\eta = 0°$, η increases counterclockwise and 'B' identifies the beam stop. The white arrow identifies a prominent, first-order *D*-period arc, and an orange arrow labels a highly directional halo of strong scattering normal to the axis of the centre of the *D*-period arcs. '$\Delta\eta$' indicates the azimuthal FWHM intensity of a *D*-period arc, and '1' and '2' label two sets of arcs in the pattern from block f (great hammerhead).

η at which the maximum *D*-period peak intensity occurs, η_{Dmax}, was quite variable (table 3) and is discussed below.

With the exception of two blocks (4 and Tg2d), the *D*-arcs remained in the same orientation for all positions in the translation scan (electronic supplementary material, videos S1–S8). The arcs for block 4 (scalloped hammerhead vertex block) rotated 30–35° (monotonically) over approximately 2.9 mm translation (electronic supplementary material, video S5). The arcs for block Tg2d (tiger shark axial block) rotated a small amount, less than 10° (electronic supplementary material, video S2).

4. Discussion

Even though the ancestors of sharks and of mammals diverged approximately 420 Ma [25], the mineralized tissue of sharks and of bones are both bioapatite nanoparticle-reinforced composite materials based on collagen matrices.

Previous studies showed shark centra and tesserae contained a bioapatite similar to that in bone [8–11,18], but quantitative data on the mineral phase (precise and accurate lattice parameters and crystallite size) and its nanoscale organization within the cartilage matrix were lacking. Given the different collagen-based matrices (bone's type I collagen fibrils—triple helices of two $\alpha1$ chains and one $\alpha2$ chain versus shark's type II collagen fibrils—triple helices of three $\alpha1$ chains [26]), one could only speculate whether there were significant differences in the two bioapatites' crystal lattice parameters, nanoparticle sizes and nanoparticle organization, characteristics which can affect tissue mechanical properties. The present study is important, therefore, because it provides the first detailed crystallographic data for the phylogenetic subclass Elasmobranchii. Further, the present WAXS/SAXS data suggest that the centrum bioapatite does not vary appreciably across the two orders sampled but does differ from bone's bioapatite.

4.1. Lattice parameters a and c; crystallite size L_c; D

The bioapatite lattice parameters of the shark centra averaged $a = 9.420 \pm 0.009$ Å and $c = 6.894 \pm 0.002$ Å. For comparison, mean bioapatite lattice parameters for bone of 10 mammalian and one avian species were $9.441 < a$ (Å) less than 9.484 and $6.895 < c$ (Å) less than 6.907 [27]; for different anatomical sites in (ancient) humans with very different body habitus, Foley *et al.* [28] reported $9.430 < a$ (Å) less than 9.443 and $6.885 < c$ (Å) less than 6.890; for archeological human second metacarpal bones, Park *et al.* [29] found $9.430 < a$ (Å) less than 9.446 and $6.878 < c$ (Å) less than 6.895. Therefore, the shark species had a slightly smaller and c slightly larger than these terrestrial species. Inorganic hAp can incorporate up to approximately 22 wt% carbonate, and an increase of 1.66 wt% carbonate produces a decrease in a of 1×10^{-2} and a much smaller increase in c [30], suggesting that shark centrum bioapatite contains somewhat more carbonate than bone. Incorporation of impurities into the bioapatite of mineralized tissue reflects the physiological conditions at the time the tissue was formed, and the difference between the shark tissue and bone may provide important clues as to differences in mineralization of cartilage (type II collagen + type I collagen + proteoglycans) versus type I collagen.

The WAXS peaks for shark centra were slightly narrower than is typically seen for bone. The c-axis crystallite sizes L_c for the shark centra tissue averaged 60 nm, larger than the approximately 40 nm typically seen by the authors (J.S.P., J.D.A. and S.R.S.) for bone, e.g. [15,29]. Further, microstrain appeared to be absent in the shark centrum whereas the authors (J.S.P., J.D.A. and S.R.S.) always see substantial microstrain in bone. Omelon *et al.* [18] published diffraction patterns from powdered shark tesserae tissue and reported c-axis crystallite size of approximately 15 nm, in comparison with cortical bone values. However, the diffraction peaks were quite weak and microstrain was not considered. Tesserae are much more mineralized than centrum tissue, and the present authors expect that microstrain would be found in shark tesserae.

One or more blocks from each species showed strong D-period arcs to either side of the beam stop. In two blocks, f and 4, two pairs of arcs were observed, and the D-period arc azimuthal orientations are interpreted below. Values of D were in the range of 67–68 nm (table 3), except for block m ($D = 64.5$ nm) where the D-period arcs were too weak for accurate measurement and block L2c where arcs were not observed. The D values for shark centra were, therefore, somewhat larger than values determined by SAXS for other mineralized tissues, e.g. D approximately 65 nm in mineralized equine articular cartilage [31] and D approximately 65 nm in human metacarpal bone [29]. Note the authors are unaware of SAXS studies of tessellated elasmobranch tissue, so it is unknown whether the D periodicity exists in this tissue.

The sample blocks were in a solution of 50% ethanol as a preservative, hardly the centra's *in vivo* environment. The authors' (S.R.S., J.D.A. and J.S.P.) past work on bone, data not shown, reveals ethanol immersion would not have changed any of the quantities measured with WAXS (lattice parameters and crystallite size) nor would this immersion change the crystallographic texture revealed by WAXS. The hydration state of the cartilage would be affected, and perhaps D, the spacing of the bioapatite nanoparticles derived from the SAXS peaks, might also change. However, the nearly 4%

difference in D between the shark centra tissue and bone (67–68 versus 65 nm) cannot be explained by this effect.

In the shark centra, the SAXS halo extends quite far along the azimuthal direction normal to that of the D-period peak maximum intensity; in fact, the halo can extend well beyond the second D-period peak (figure 4a) and much farther than halos in bone SAXS patterns. The axis of the SAXS halo indicates the direction of the smallest dimension of the scatterers producing the halo [32]; this size is much smaller than D. For bone and dentin, the smallest dimension of the bioapatite particles (halo direction) is well known to be perpendicular to the nanocrystals' maximum length along the unit cell c-direction [33]. In the shark centra, like in bones, the scatterers are bioapatite nanoparticles, but the WAXS and SAXS data do not reveal whether the shark centra particles are nanoscale needles or plates; normally one must rely on techniques such as transmission electron microscopy to make this distinction.

4.2. Crystallographic texture

Over the sample positions studied and the range of azimuths sampled for axially oriented block Tg2d, the intensity of the 00.4 diffraction ring varied significantly: there was a monotonic increase in intensity from $\eta = 180°$ to $130°$. The azimuthal 00.4 intensity variation was also present in the other five blocks of this study. Constraints of running under COVID-19 protocols, dictated that only one GE detector panel was used. Given the resulting limit of WAXS azimuthal coverage with one detector panel positioned to the side of the incident beam (so that SAXS could be collected simultaneously), the texture of the mineral phase is best discussed using the SAXS data.

The azimuthal FWHM of the sharks' D-period arcs (25–30°) is much narrower than those the authors (S.R.S., J.S.P. and J.D.A.) typically measure for human, canine and bovine cortical bone (approx. 60–70° [15,23,29]). In the present study, the X-ray beam averages over approximately 3 mm of tissue thickness and, if microstructure varies along the beam path, it is possible that the shark nanoparticles are even more tightly aligned than is apparent from these data. The higher alignment of bioapatite nanoparticles (and underlying cartilage) in shark tissue than in bone (and its type I collagen) could be intrinsic to the different matrices (cartilage, a mixture of types I and II collagen and proteoglycans, versus type I collagen), but further work would be required to establish or refute this relationship. Too little is known about shark cartilage (mineralized and unmineralized) to inform the present discussion, but mammalian articular cartilage (which consists of mineralized and unmineralized zones) is highly aligned to resist loading and it is not unreasonable to hypothesize that the relatively tight nanoparticle alignment (compared with bone) reveals something important about microstructural patterns of loading. The SAXS halo, like the D-period peaks, has a much narrower azimuthal range than that seen in bone.

Visual inspection of blocks Tg2c and Tg2d reveals that most of the length of the blocks is unmineralized cartilage (the gap region in figure 2a, red arrows). However, the volumes at each end of these blocks consist of cone wall material, and this mineralized tissue occupies the entire cross-section. Electronic supplementary material, videos S1 and S2 show that all of the SAXS patterns recorded in the scan across block Tg2c (spanning about 2.44 mm) and

across Tg2d (spanning about 2.46 mm) appear similar to that in figure 5 (upper left SAXS pattern), and this demonstrates that the Tg2c and Tg2d patterns are from the cone wall. For blocks Tg2c and Tg2d, the axis of the pair of D-period arcs are roughly normal to the axis of the centrum, with the deviation from 90° being attributable to tilt of the blocks within the tubes. In other words, the bioapatite c-axes of the tiger shark cone walls are perpendicular to the vertebral column axis, in agreement with EDD mapping results for a blue shark centrum [11,12] (another carcharhiniform). The SAXS pattern of L2d (figure 5) also appears to be from cone wall material and has the same c-axis orientation.

In additional to the results on the bioapatite cone wall texture, Park et al. [12] and Stock et al. [11] found that the intermedialia bioapatite also contained strong crystallographic texture, with c-axes being oriented along the centrum axis, i.e. at 90° to that in the cone walls. Because the axis of the D-period arcs for block 9 (scalloped hammerhead) is parallel to the centrum axis, the present authors identify these patterns as being from the intermedialia. The patterns from blocks 4 (scalloped hammerhead) and f (great hammerhead) have two sets of D-period arcs, whose axes are azimuthally 90° apart. The sampled tissue apparently contains both intermedialia and cone wall material.

Some of the SAXS data demonstrate that the centra's crystallographic texture has gradients beyond the simple cone wall/intermedialia differences noted by [11,12]. The D-period arcs for two blocks (4 and Tg2d) rotate azimuthally with position (electronic supplementary material, video S2 and S5) by 30–35° over approximately 2.9 mm translation and less than 10°, respectively. Spatial gradients in texture between intermedialia and cone is not unexpected and is consistent with curvature of intermedialia growth bands [4,22,34]. Additional scattering studies designed to map texture on the 50–100 μm scale would be very informative, for example, reconstructing virtual slices through similar-sized centrum blocks using WAXS/SAXS tomography [35,36] or mapping carefully selected thin sections [20]. The EDD maps of intact centra [11,12] lack the spatial and azimuthal angle resolutions required to quantify texture gradients, and the EDD instrument does not sample the small-angle regime. The WAXS/SAXS approach is complementary, therefore, to the EED approach and might even be extended to intact centra using conical [37] or spiral slits [38].

4.3. Implications of the small-angle X-ray scattering/ wide-angle X-ray scattering observations for centra mechanical functionality

Vertebrae's responses to in vivo loading can be simulated numerically by combining geometry with tissue properties or can be measured experimentally, e.g. [5,7]. The present WAXS/SAXS data relate to tissue-level constitutive properties which might be useful in modelling or in inferring tissue properties via analogy with similar mineralized tissues. Experimental three-dimensional X-ray-scattering-based strain mapping is outside the scope of this paper, but these methods are related to the WAXS/SAXS data and are discussed at the end of this subsection.

The present WAXS/SAXS data show that the bioapatite mineral and its nanostructural organization (lattice parameters a and c, crystallite size L_c, nanoparticle spacing D, crystallographic texture) vary little, on the average, across the orders Lamniformes and Carcharhiniformes. The limited data also suggest that bioapatite added early in the shark's lifetime (closer to the centrum axis) does not differ significantly from material added later: bioapatite characteristics for radially adjacent blocks (tiger shark and porbeagle shark) and for a vertex block (scalloped hammerhead) are virtually identical. More specimens from more species need to be studied, however, before this tentative conclusion is firmly established. Even if each centrum's mean bioapatite lattice parameters/crystallite sizes do not change with age, lattice parameters/crystallite sizes may oscillate about the mean values, i.e. at different positions within each growth band, as was seen across other mineralized tissues' growth bands [20]. The present experiments collected a single average WAXS pattern for each block, and a differently designed WAXS study is required to address this latter possibility.

Macrostructure, microstructure and tissue-level mechanical properties all contribute to functionality of hierarchically structured mineralized tissues such as bone [19], shark tesserae [13,39–41] and shark centra [2,4]. Despite recent additions to the literature on the mineralized cartilage of shark centra, e.g. [2,4,5,7,8,11,12,22,34], this tissue remains much less investigated than bone or tessellated tissue. Although shark tesserae are the closest mineralized tissue to those of centra tissue, tesserae contain just under 10 vol% soft tissue/porosity [41] whereas centra cones contain approximately 60 vol% and centra intermedialia approximately 75 vol% soft tissue/porosity [11], suggesting that it would be inaccurate to extrapolate centra tissue materials properties from tesserae data. Centrum bioapatite mineral's lattice parameters a and c, crystallite size L_c and nanoparticle spacing D are close enough to those of bone (less than 1% and less than 5% differences for lattice parameters and D, respectively, and L_c 50% larger than that the authors typically measure for bone at this beam line but within the range reported for bone), that it may be possible, as a zero-order approximation, to extrapolate trends observed in bone tissue to shark centrum tissue. Two examples are Young's modulus increase as bone mineral content rises [42] and Young's moduli increase along anatomical directions with strong c-axis preferred orientation [21].

Previously published three-dimensional EDD maps of an entire blue shark (carcharhiniform) centrum showed the bioapatite c-axes within the cone walls were perpendicular to the vertebral column axis, and the c-axes within the intermedialia were parallel to the vertebral column axis [11,12], and produced the hypothesis that the two c-axis orientations (and the co-oriented cartilage fibrils) serve different functions: in the cone wall, the c-axes were aligned to resist radial deflection of the cone walls, thereby constraining the fluid-filled intervertebral capsule, and, in the intermedialia, to resist axial compression and to support the cone walls [11,12]. The present observations of D-period arc orientations of the cone wall and intermedialia are consistent with the blue shark observations, extend the earlier observations to additional carcharhiniform and lamniform species and suggest that the pattern of two orthogonal textures within the cone walls and intermedialia may be a basal character of mineralized shark centra. Further investigation is needed, especially of the spatial gradients in texture observed in two blocks.

One can imagine three-dimensional numerical models of centra under load based on microCT-derived geometry (e.g. [4]) and on directionally dependent Young's moduli. Such a model would allow virtual testing in simple compression and also in bending. MicroCT-based three-dimensional

modelling is a standard approach with bone [43–45]. Recently, a preliminary EDD strain mapping report appeared on *in situ* loading of an intact carcharhiniform centrum [46], and it appears that this approach will provide valuable insight. One expects comparison of actual three-dimensional strain maps with results of numerical modelling will advance understanding of shark centrum functionality.

Mineralized cartilage also occurs in mammalian joints, its microstructure is well known, e.g. [47]. SAXS has revealed *D*-period peaks from articular cartilage similar to those of bone [31], and WAXS from this cartilage appears similar to bone [48]. This suggests that it would be fruitful to study shark centra with techniques like those applied to mammalian cartilage and that insights gained into shark centra cartilage might apply to the mammalian cartilage and bone and vice versa.

Endnotes

[1] For human femoral cortical bone, Martin *et al.* [6] estimate that bone will fail at 9.3×10^6 cycles at peak physiological compressive strain of 0.2%.

[2] Here the abbreviated Miller-Bravais indexing system is used to emphasize the hexagonal crystal system of hAp and of the bioapatite [13].

[3] Note that the Miller-Bravais indexing system ($hkil$ where $-i=h+k$) is used in its abbreviated form $hk.l$ to emphasize the hexagonal crystal system [14].

[4] Here and elsewhere quantities following "±" are the standard deviation of the mean.

References

1. Rama S, Chandrakasan G. 1984 Distribution of different molecular species of collagen in the vertebral cartilage of the shark (*Carcharius acututs*). *Conn. Tiss. Res.* **12**, 111–118. (doi:10.3109/03008208408992776)

2. Porter ME, Beltran JL, Koob TJ, Summers AP. 2006 Material properties and biochemical composition of mineralized vertebral cartilage in seven elasmobranch species (Chondrichthyes). *J. Exp. Biol.* **209**, 2920–2928. (doi:10.1242/jeb.02325)

3. Watanabe YY, Lydersen C, Fisk AT, Kovacs KM. 2012 The slowest fish: swim speed and tail-beat frequency of Greenland sharks. *J. Exp. Mar. Biol. Ecol.* **426/427**, 5–11. (doi:10.1016/j.jembe.2012.04.021)

4. Morse PE, Stock MK, James KC, Natanson LJ, Stock SR. 2022 Shark vertebral microanatomy and mineral density variation studied with laboratory microComputed Tomography. *J. Struct. Biol.* **214**, 107831. (doi:10.1016/j.jsb.2022.107831)

5. Porter ME, Diaz C, Sturm JJ, Grotmol S, Summers AP, Long JHJr. 2014 Built for speed: strain in the cartilaginous vertebral columns of sharks. *Zoology* **117**, 19–27. (doi:10.1016/j.zool.2013.10.007)

6. Martin RB, Burr DB, Sharkey NA. 1998 *Skeletal tissue mechanics*. New York, NY: Spinger Verlag.

7. Ingle DI, Natanson LJ, Porter ME. 2018 Mechanical behavior of shark vertebral centra at biologically relevant strains. *J. Exp. Biol.* **221**, 188318. (doi:10.1242/jeb.188318)

8. Dean MN, Summers AP. 2006 Mineralized cartilage in the skeleton of chondrichthyan fishes. *Zoology* **109**, 164–168. (doi:10.1016/j.zool.2006.03.002)

9. Urist MR. 1961 Calcium and phosphorus in the blood and skeleton of the Elasmobranchii. *Endocrinol* **69**, 778–801. (doi:10.1210/endo-69-4-778)

10. Dean MN, Chiou WA, Summers AP. 2005 Morphology and ultrastructure of prismatic calcified cartilage. *Microsc. Microanal.* **11**, 1196–1197.

11. Stock SR et al. 2022 Microstructure and energy dispersive diffraction reconstruction of 3D patterns of crystallographic texture in a shark centrum. *J. Med. Imaging* **9**, 031504. (doi:10.1117/1.JMI.9.3.031504)

12. Park JS, Chen H, James KC, Natanson LJ, Stock SR. Submitted. Three-dimensional mapping of mineral in intact shark centra with energy dispersive X-ray diffraction. *J. Mech. Behav. Biomed. Mater.*

13. Seidel R, Jayasankar AK, Dean MN. 2021 The multiscale architecture of tessellated cartilage and its relation to function. *J. Fish Biol.* **98**, 942–955. (doi:10.1111/jfb.14444)

14. Cullity BD, Stock SR. 2001 *Elements of X-ray diffraction*, 3rd edn. Upper Saddle River, NJ: Prentice-Hall.

15. Almer JD, Stock SR. 2005 Internal strains and stresses measured in cortical bone via high-energy X-ray diffraction. *J. Struct. Biol.* **152**, 14–27. (doi:10.1016/j.jsb.2005.08.003)

16. Henney GC, Spiegel-Adolf M. 1945 X-ray diffraction studies on fish bones. *Am. J. Physiol.* **144**, 632–636. (doi:10.1152/ajplegacy.1945.144.4.632)

17. Zhou HW, Burger C, Wang H, Hsiao BS, Chu B, Graham L. 2016 The supramolecular structure of bone: X-ray scattering analysis and lateral structure modeling. *Acta Cryst.* **D72**, 986–996. (doi:10.1107/S2059798316011864)

18. Omelon S, Georgiou J, Variola F, Dean MN. 2014 Colocation and role of polyphosphates and alkaline phosphatase in apatite biomineralization of elasmobranch tesserae. *Acta Biomater.* **10**, 3889–3910. (doi:10.1016/j.actbio.2014.06.008)

19. Weiner S, Wagner HD. 1998 The material bone: structure-mechanical function relations. *Annu. Rev. Mater. Sci.* **28**, 271–298. (doi:10.1146/annurev.matsci.28.1.271)

20. Ryan J, Stulajter MM, Okasinski JS, Cai Z, Gonzalez GB, Stock SR. 2020 Carbonated apatite lattice parameter variation across incremental growth lines in teeth. *Materialia* **14**, 100935. (doi:10.1016/j.mtla.2020.100935)

21. Guo XE. 2001 Mechanical properties of cortical bone and cancellous bone tissue. In *Bone mechanics handbook*, 2nd edn (ed. SC Cowin), pp. 10-1–10-23. Boca Raton, FL: CRC Press.

22. Natanson LJ, Skomal GB, Hoffmann SL, Porter MF, Goldman KJ, Serra D. 2018 Age and growth of sharks: do vertebral band pairs record age? *Mar. Freshw. Res.* **69**, 1440–1452. (doi:10.1071/MF17279)

23. Stock SR, Laugesen M, Birkedal H, Jakus A, Shah R, Park JS, Almer JD. 2019 Precision lattice parameter determination from transmission diffraction of thick specimens with irregular cross sections. *J. Appl.*

Cryst. **52**, 40–46. (doi:10.1107/S1600576718017132)

24. Free R, DeRocher KD, Xu R, Joester D, Stock SR. 2020 A method for mapping submicron-scale crystallographic order/disorder applied to human tooth enamel. *Powder Diffr.* **35**, 117–123. (doi:10.1017/S0885715620000251)

25. Coates MI, Finarelli JA, Sansom IJ, Andreev PS, Criswell KE, Tietjen K, Rivers ML, La Riviere PJ. 2018 An early chondrichthyan and the evolutionary assembly of a shark body plan. *Proc. R. Soc. B* **285**, 20172418. (doi:10.1098/rspb.2017.2418)

26. Hulmes DJS. 2008 Collagen diversity, synthesis and assembly. Chapter 2 In *Collagen − structure and mechanics* (ed. P Fratzl), pp. 15–47. New York, NY: Springer.

27. Beckett S, Rogers KD, Clement JG. 2011 Interspecies variation in bone mineral behavior upon heating. *J. Forensic Sci.* **56**, 571–579. (doi:10.1111/j.1556-4029.2010.01690.x)

28. Foley B, Greiner M, McGlynn G, Schmahl WM. 2020 Anatomical variation of human bone bioapatite crystallography. *Crystals* **10**, 859. (doi:10.3390/cryst10100859)

29. Park JS, Laugesen M, Mays S, Birkedal H, Almer JD, Stock SR. In press. Intact archeological human bones studied with transmission X-ray diffraction and small angle X-ray scattering. *Int. J. Osteoarchaeol.* (doi:10.1002/oa.3053)

30. Zapanta-Legeros R. 1965 Effect of carbonate on the lattice parameters of apatite. *Nature* **206**, 403–404. (doi:10.1038/206403a0)

31. Moger CJ, Barrett R, Bleuet P, Bradley DA, Ellis RE, Green EM, Knapp KM, Muthuvelu P, Winlove CP. 2007 Regional variations of collagen orientation in normal and diseased articular cartilage and subchondral bone determined using small angle X-ray scattering (SAXS). *Osteoarthr. Cartil.* **15**, 682–687. (doi:10.1016/j.joca.2006.12.006)

32. Gupta HS, Wagemaier W, Zickler GA, Hartmann J, Funari SS, Roschger P, Wagner HD, Fratzl P. 2006 Fibrillar level fracture in bone beyond the yield point. *Int. J. Fracture* **139**, 425–436. (doi:10.1007/s10704-006-6635-y)

33. Tesch W, Vandenbos T, Roschger P, Fratzl-Zelman N, Klaushofer K, Beertsen W, Fratzl P. 2003 Orientation of mineral crystallites and mineral density during skeletal development in mice deficient in tissue nonspecific alkaline phosphatase. *J. Bone Miner. Res.* **18**, 117–125. (doi:10.1359/jbmr.2003.18.1.117)

34. Geraghty PT, Jones AS, Stewart J, Macbeth WG. 2012 Micro-computed tomography: an alternative method for shark aging. *J. Fish Biol.* **80**, 1292–1299. (doi:10.1111/j.1095-8649.2011.03188.x)

35. Stock SR, De Carlo F, Almer JD. 2008 High energy X-ray scattering tomography applied to bone. *J. Struct. Biol.* **161**, 144–150. (doi:10.1016/j.jsb.2007.10.001)

36. Birkbak ME, Nielsen IG, Frolich S, Stock SR, Kenesei P, Almer JD, Birkedal H. 2017 Concurrent determination of nanocrystal shape and amorphous phases in complex materials by diffraction scattering computed tomography. *J. Appl. Crystal* **50**, 192–197. (doi:10.1107/S1600576716019543)

37. Park JS, Lienert U, Dawson PR, Miller MP. 2013 Quantifying three-dimensional residual stress distributions using spatially-resolved diffraction measurements and finite element based data reduction. *Exp. Mech.* **53**, 1491–1507. (doi:10.1007/s11340-013-9771-0)

38. Martins RV, Ohms C, Decroos K. 2010 Full 3D spatially resolved mapping of residual strain in a 316L austenitic stainless steel weld specimen. *Mater. Sci. Eng. A* **527**, 4779–4787. (doi:10.1016/j.msea.2010.03.110)

39. Liu X, Dean MN, Youssefpour H, Summers AP, Earthamn JC. 2014 Stress relaxation behavior of tesselated cartilage from the jaws of blue sharks. *J. Mech. Behav. Biomed. Mater.* **29**, 68–80. (doi:10.1016/j.jmbbm.2013.08.014)

40. Seidel R *et al.* 2019 Mechanical properties of stingray tesserae: high-resolution correlative analysis of mineral density and indentation moduli in tessellated cartilage. *Acta Biomater.* **96**, 421–435. (doi:10.1016/j.actbio.2019.06.038)

41. Chaumel J, Schotte M, Bizzarro JJ, Zaslansky P, Fratzl P, Baum D, Dean MN. 2020 Co-aligned chondrocytes: zonal morphological variation and structures arrangement of cell lacunae in tessellated cartilage. *Bone* **134**, 115624. (doi:10.1016/j.bone.2020.115264)

42. Currey JD. 2002 *Bones − structure and mechanics*. Princeton, NJ: Princeton University Press.

43. Kinney JH, Haupt DL, Balooch M, Ladd AJC, Ryaby JT, Lane NE. 2000 Three-dimensional morphometry of the L6 vertebra in the ovariectomized rat model of osteoporosis: biomechanical implications. *J. Bone Miner. Res.* **15**, 1981–1991. (doi:10.1359/jbmr.2000.15.10.1981)

44. Niebur GL, Feldstein MJ, Yuen JC, Chen TJ, Keaveny TM. 2000 High-resolution finite element models with tissue strength asymmetry accurately predict failure of trabecular bone. *J. Biomech.* **33**, 1575–1583. (doi:10.1016/S0021-9290(00)00149-4)

45. van Rietbergen B. 2001 Micro-FE analyses of bone − state of the art. In *Noninvasive assessment of trabecular bone architecture and the competence of bone* (eds B.K. Bay, S Majumdar). New York, NY: Kluwer/Plenum. *Adv. Exp. Med. Biol.* **496**, 21–30.

46. Park JS, Chuang AC, Okasinski J, Chen H, Shade P, Stock SR, Almer J. In press. A new residual strain mapping program using energy dispersive X-ray diffraction at the Advanced Photon Source. *Exp. Mech.* (doi:10.1007/s11340-022-00859-1)

47. Hall BK. 2005 *Bones and cartilage: developmental and evolutionary skeletal biology*. Amsterdam, The Netherlands: Elsevier.

48. Duer MJ, Friscic T, Murray RC, Reid DG, Wise ER. 2009 The mineral phase of calcified cartilage: its molecular structure and interface with the organic matrix. *Biophys. J.* **96**, 3372–3378. (doi:10.1016/j.bpj.2008.12.3954)

49. Park JS, Almer JD, James KC, Natanson LJ, Stock SR. 2022 Bioapatite in shark centra studied by wide angle and by small angle X-ray scattering. Materials Data Facility. (doi:10.18126/snb5-r5pf)

50. Park JS, Almer JD, James KC, Natanson LJ, Stock SR. 2022 Bioapatite in shark centra studied by wide angle and by small angle X-ray scattering. Figshare. (doi:10.6084/m9.figshare.c.6189313)